Scripta Materialia 170 (2019) 177–182

Contents lists available at ScienceDirect

Scripta Materialia

journal homepage: www.elsevier.com/locate/scriptamat

Correlation between cell wall buckling and deformation banding in a closed-cell foam

H.W. Chai[a], H.Y. Li[b,c], X.H. Xiao[d], J.Y. Huang[a,b,c,*], S.N. Luo[a,b,c,*]

[a]The Peac Institute of Multiscale Sciences, Chengdu, Sichuan 610031, PR China
[b]Key Laboratory of Advanced Technologies of Materials, Ministry of Education, Southwest Jiaotong University, Chengdu, Sichuan 610031, PR China
[c]Institute of Materials Dynamics, Southwest Jiaotong University, Chengdu, Sichuan 610031, PR China
[d]Advanced Photon Source, Argonne National Laboratory, Argonne, IL 60439, USA

ARTICLE INFO

Article history:
Received 25 April 2019
Received in revised form 31 May 2019
Accepted 3 June 2019
Available online 19 June 2019

Keywords:
X-ray tomography
Closed-cell foam
Deformation banding
Microstructural evolution

ABSTRACT

We investigate deformation dynamics in a widely used closed-cell foam of polymethacrylimide under uniaxial compression with *in situ* X-ray computed tomography and digital volume correlation. Axial strain mapping demonstrates discrete deformation bands nucleated in sequence across the sample. A buckling strength index is proposed to quantify the buckling resistance of cell walls, based on their morphology extracted via an edge-segmentation procedure developed in this work. The spatial distribution of the weakest cell walls is correlated well with the location and nucleation sequence of deformation bands, and can be used for predicting deformation banding.

Cellular materials can be made of a wide variety of materials, including metals, ceramics, and polymers, and exhibit excellent physical, mechanical and biological properties [1-3]. They are being increasingly used in various engineering applications for energy absorption, catalysis, sandwich structures and/or tissue repair [3,4]. Understanding the relationship between microstructures of cellular materials and their mechanical properties (in particular deformation and failure) is of substantial interest [5]. However, exploring deformation mechanisms at the cell scale has been an experimental challenge.

Deformation of cellular materials under compression begins with elastic deformation of the cellular structure, followed by local collapse of cells via elastic or plastic buckling. During the collapse stage, deformation proceeds in a strongly localized manner within narrow crushing bands that nucleate and propagate within the cellular structure [6], as manifested by optical digital image correlation (DIC) [7-9]. The formation of localized compaction bands is considered universal to cellular materials and cohesive granular materials (e.g., porous sandstone [10] and snow [11]).

An important but pending question is what structural factors trigger the localized collapse of cells. Considerable efforts have been made to predict the location of deformation bands in cellular materials based on their microstructures [12,13], e.g., local density and cell size. It was proposed that deformation banding can be detected with measures of structural anisotropy [12] quantified via the Minkowski tensor analysis [14]. However, the increase in local anisotropy shown in previous data [12] is not pronounced. X-ray computed tomography (CT) showed that cells which exhibit the most visible distortions are not the largest, but are those elliptic non-equiaxed [15]. It implies that the cell morphology might dominate its deformation and failure over the cell size. However, 3D quantification on the morphology of cells (especially cell walls) is rarely reported, which hinders understanding the correlation between cell morphology and deformation banding. In addition, deformation band angles were previously characterized with two-dimensional (2D) DIC [7]. However, deformation bands in real foams are inherently 3D, and accurate characterization of band morphology with 3D CT is critical for validating constitutive models of foams [7].

With synchrotron sources, *in situ* CT has been developed to characterize the evolution of 3D cellular structures [13,16-19]. Micro CT facilitates characterization of cell deformation at a micron scale [20]. In this letter, uniaxial compression tests are carried out on a representative closed-cell foam, polymethacrylimide (PMI) foam. PMI foams are superior to conventional polymer foams in mechanical properties [21,22]. Here, *in situ* synchrotron CT is adopted to map 3D microstructures of PMI foams. A new image processing technique is proposed to quantify cell wall morphology. The buckling strength

* Corresponding authors at: The Peac Institute of Multiscale Sciences, Chengdu, Sichuan 610031, PR China.
E-mail addresses: jyhuang@pims.ac.cn (J. Huang), sluo@pims.ac.cn (S. Luo).

https://doi.org/10.1016/j.scriptamat.2019.06.006
1359-6462/

index is calculated for cell walls based on the elastic buckling theory. The spatial distribution of the strength index allows for the prediction of deformation bands.

The initial density of the PMI foam is 52 kg m^{-3}, measured with a 100 × 100 × 60 mm^3 foam block. The solid fraction of the foam is calculated as 4.3% on the basis of the apparent density of the foam sample and the solid PMI density (1200 kg m^{-3}). The as-received foam block is machined into cuboidal samples via laser cutting. The sample size is 3.5 × 3.5 × 4.0 mm^3, and the sample height (along the loading direction) is 4.0 mm. The sample contains over 10 cell layers in both the longitudinal and horizontal directions, sufficient for mechanical analysis of the PMI foams [15].

A miniature material test system (MTS) is designed for *in situ* CT experiments at the beamline 2-BM of the Advanced Photon Source. More experimental details can be found in Ref. [20]. The X-ray energy is set at 24.9 keV, and the sample-to-scintillator distance, at 60 mm. The nominal resolution is 0.87 μ m per pixel. The projection data for each tomography scan comprise 1500 radiographs in 0°–180°, which are then reconstructed into volume data using an open-source program TomoPy [23]. To quantify the 3D structures of foams, the volume data is binarized via the level set method after thresholding segmentation [24]. The threshold is selected to yield the solid fraction of foams (~0.045) consistent with prior measurement. Since the wall thickness in PMI foams is only a few voxels at certain locations, local watershed segmentation [25] is applied to recover those thin walls which may have been wrongly removed during the global binarization process.

The samples are scanned at different strain levels including zero strain. The stress–strain curves are measured simultaneously with the MTS device. Upon loading, once the desired strain level is achieved, the upper platen is fixed and CT-scan is carried out after the stress relaxes to a nearly stable state. Since the sample height is larger than the field of view (1.8 mm high), two or three scans are necessary to cover the whole gauge length at each deformation stage. For two consecutive scans, there is an overlap of ~0.34 mm along the loading direction. Such an overlap facilitates the splicing

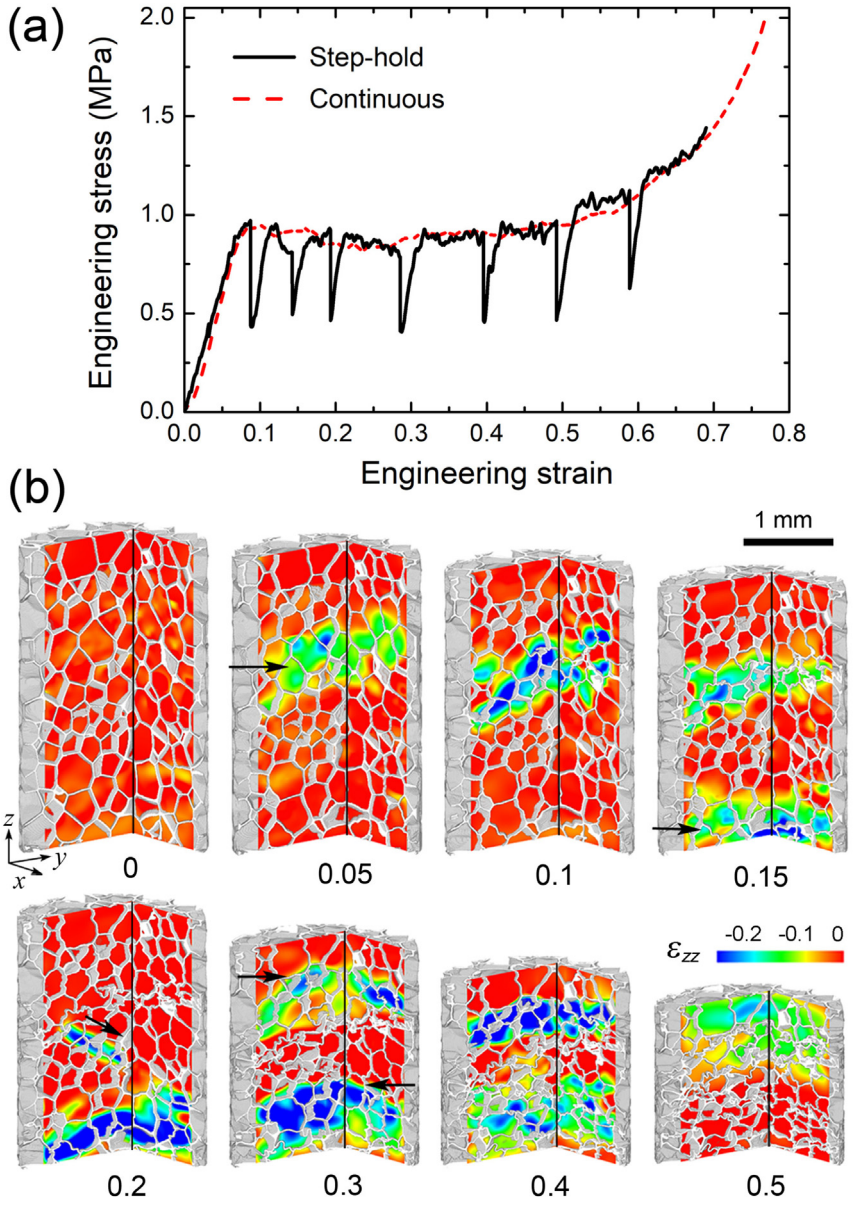

Fig. 1. (a) Stress–strain curves of the PMI foam under uniaxial compression. The solid curve with stress drops refers to *in situ* CT test with pauses, while the dashed curve, to continuous loading. (b) Volume renderings of the PMI foam at different bulk strains obtained from *in situ* CT measurements. Color-coding refers to the increment in axial strain between two consecutive images.

of two sets of volume data in post-processing using the normalized cross-correlation method [26].

The engineering stress–strain curves along with the 3D volume renderings are presented in Fig. 1. The solid curve with stress drops is the stress–strain curve from the *in situ* CT test with loading pauses. For comparison, a continuous loading test is also conducted (the dashed curve); the stress–strain curves in these two cases agree well. The initial volume rendering indicates that cells are largely polyhedrons; the foam is nearly isotropic with no preferred cell orientations; the equivalent diameter of cells is distributed in a narrow range of 200–400 μm with a mean of 323 μm.

The axial strain fields (ε_{zz}) are calculated via digital volume correlation (DVC) [16,27], and Fig. 1 (b) shows the *xz*- and *yz*-cross-sections of the 3D strain maps. Correlation is calculated between two adjacent tomographs and a strain map is overlaid on the previous tomograph. At the elastic stage, the foam sample deforms via the elastic deformation of the foam skeleton, yielding a uniform strain field with low amplitudes. During the collapse stage, deformation banding occurs and significant cell collapse and crushing are observed within the bands. Compressional strain localizations develop at 10% strain due to cell wall bending and buckling, and subsequently, an apparent collapse band appears at 15% strain. With increasing loading, discrete deformation bands are formed in sequence (marked by arrows in Fig. 1 (b)). Strain localizations in the nucleated bands fade out with further loading, due to local densification or hardening. At about 60% strain, all deformation bands coalesce, resulting in macroscopic densification of the sample.

The wrinkles or folds in cells are selected to characterize deformation bands. The band angle θ and the azimuthal angle ψ are calculated via planar fitting. θ is the angle between the loading direction and a band normal; ψ is the angle between the projection of a band normal on the *xy*-plane and the *x*-axis. Fig. 2 (a) presents the deformation band distribution across the sample at 40% strain. Five deformation bands (E1–E5) initiated at different instants are singled out for analysis. Evolutions of the θ and ψ values of deformation bands with bulk strain are shown in Fig. 2 (b). The initiation band angles for bands E2–E4 (~10°) are similar, but larger than those for bands E1 (8°) and E5 (4°), probably due to the structural inhomogeneity across the sample. The band angle decreases with increasing loading, as illustrated by the exponential decay curve. The initiation azimuthal angle and its evolution are quite different for five bands, partly due to the complexity incurred by the 3D nature of the deformation bands.

For comparison with Saadatfar et al. [12], we also calculate the distribution of the Minkowski anisotropic index, $\beta_2^{0,2}$ [14], along the loading direction (Fig. S1). A lower $\beta_2^{0,2}$ value means higher local structural anisotropy. The initial $\beta_2^{0,2}$ value is around 0.95 and does not show strong variation along the sample height, indicating an initial isotropy. As marked by arrows in Fig. S1, $\beta_2^{0,2}$ exhibits an apparent decrease only in the vicinity of deformation bands, but no obvious reduction (i.e. increase in anisotropy) in these areas prior to band nucleation. Therefore, the increase in local anisotropy is a result of cell deformation and collapse, rather than a signal of deformation band nucleation.

Tomographic images (Fig. 1 (b)) show that cell collapse is generally preceded by (elastic) buckling of cell walls. Therefore, it is essentially the buckling strength of cell walls that dominates cell collapse and subsequent deformation band nucleation. We propose a buckling strength index in terms of cell wall morphology under two assumptions: (I) cell walls are simply supported by neighboring walls; and (II) cell walls are subjected to elastic buckling. According to the elastic buckling theory for thin plates [28], the critical buckling strength σ_{cr} of a plate compressed by a uniform stress field and with four edges supported (Fig. S2(a)), is

$$\sigma_{cr} = \frac{\pi^2 E_s}{12\,(1-\nu_s^2)} K \frac{t^2}{b^2}, \tag{1}$$

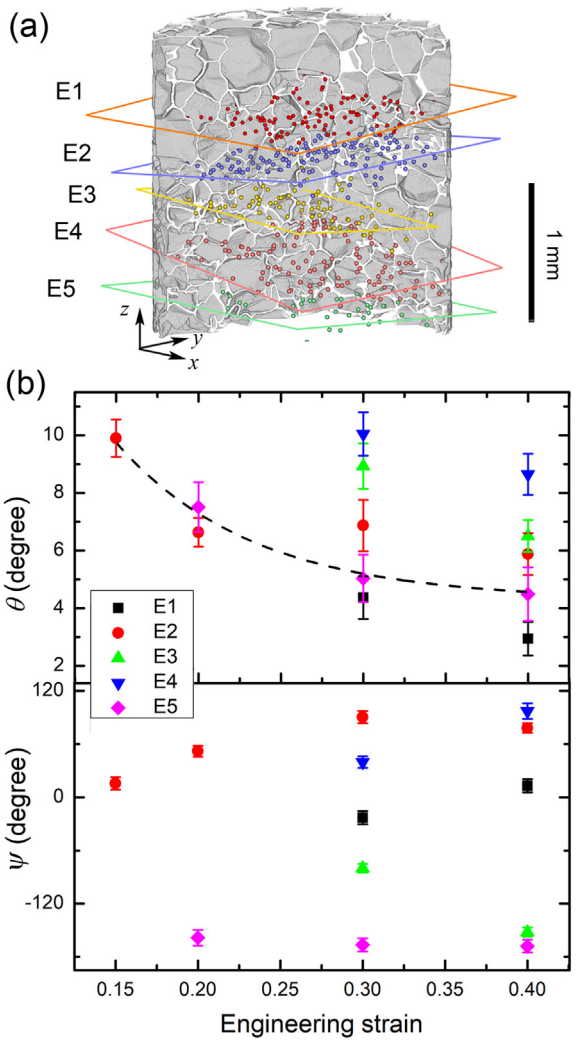

Fig. 2. (a) Deformation bands (E1–E5) in the foam sample at 40% strain. Wrinkles (denoted with dots) in cell walls are selected to extract deformation bands via planar fitting. (b) Evolution of the band angle θ and the azimuthal angle ψ, of deformation bands with bulk strain. θ: the angle between the loading direction and a band normal; ψ: the angle between the projection of a band normal on the *xy*-plane and the *x*-axis.

where E_s and ν_s are the elastic modulus and Poisson's ratio of the plate, respectively. K is the elastic buckling coefficient. $K = (b/h + h/b)^2$ for $h/b \le \sqrt{2}$, and $K = 4$ for $h/b > \sqrt{2}$. t, b and h are the thickness, width and height of the plate, respectively.

Suppose that cell walls are randomly orientated with respect to the loading direction. The angle between the loading direction and a wall normal is denoted as β (Fig. S2(b)). We also assume that the stress imposed on each wall (σ_m) is along the loading direction (Fig. S2(b)). The stress component parallel to the wall, $\sigma_m \sin\beta$, induces the buckling of wall. A strength index λ_w for evaluating the buckling resistance of a cell wall is then proposed as

$$\lambda_w = K(h_w, b_w)\frac{t_w^2}{b_w^2}\frac{1}{\sin\beta}, \tag{2}$$

where t_w, b_w and h_w are the thickness, equivalent width and height of the cell wall, respectively, as defined in Fig. S2(b).

To obtain geometric parameters of cell walls, we develop a new technique for edge segmentation, i.e. separating cell edges and walls, as illustrated in Fig. 3. In a binary 2D slice (e.g. the *xy*-slice, Fig. 3 (a)), cell walls become lines, while edges become corners or lines

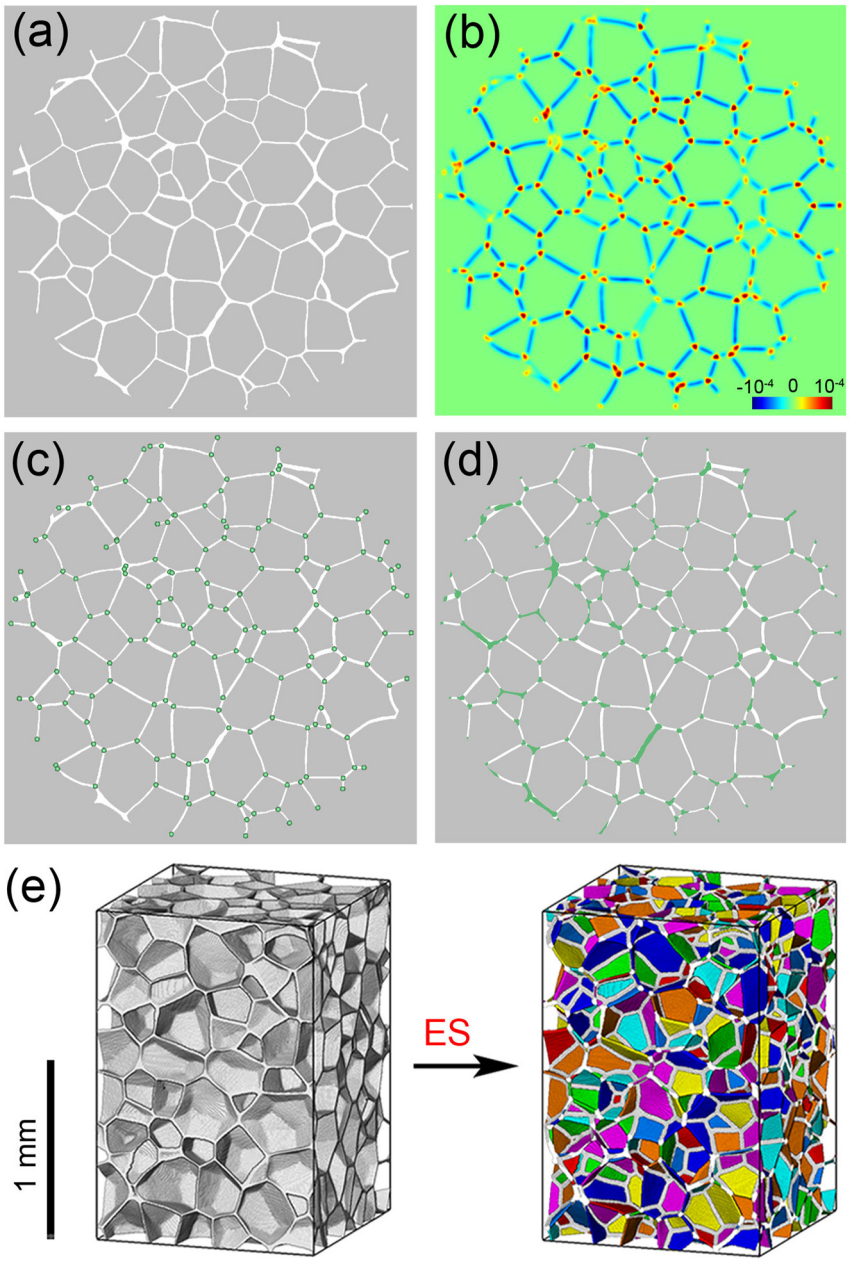

Fig. 3. Procedure for edge segmentation. (a) A binary slice in the *xy*-plane. (b) Corresponding mapping of the Harris operator value. (c) Corner center or edge core voxel distribution for edges not parallel to the *xy*-plane. (d) Edge voxel distribution in the *xy* slice. (e) The foam configurations before and after edge segmentation (ES).

(for the edges parallel to the *xy*-plane). Then, the 2D Harris corner detector algorithm [29] is applied to the slice to extract the corner regions. The Harris operator value, $h(x,y)$, is calculated and assigned to each voxel on the slice (Fig. 3 (b); represented by color-coding). $h(x,y)$ can be positive, negative or zero, referring to the cases where a voxel belongs to a corner region, a line or a flat region, respectively. The corner region contains a number of voxels depending on the edge thickness. It is impossible to accurately obtain the whole corner region via simply thresholding with $h(x,y)$.

A feasible way is as follows. We first choose the center of a corner region (i.e. the edge core; green dots in Fig. 3 (c)) according to the local maximum of $h(x,y)$. Then the procedure shown in (a)–(c) is repeated for all the *xy*-, *xz*- and *yz*-slices to obtain all edge cores in the volume. Finally, each edge core is expanded into a sphere with a given radius, and the edges are the intersection voxels between the spheres and the volume data. The radius is set empirically at 9.5 voxels, which can extract the majority of edges and segment the walls connected to them. Local watershed segmentation is applied manually to separate those walls with very thick edges (radius > 9.5 voxels). Fig. 3 (d) illustrates the edge voxels (colored green) located in the *xy*-slice. The voxels outside the edges consists of the cell walls which are separated from each other via the connectivity criterion. The foam sample after edge segmentation (Fig. 3 (e)) is separated into an edge skeleton (white) and 2352 walls (color). The solid fraction in edges (edge volume divided by the total solid volume) is estimated as ~0.3, much lower than those in conventional polymer foams (~0.8 [1]) with curved, thin cell walls. This may contribute to the difference in the dominant deformation modes at

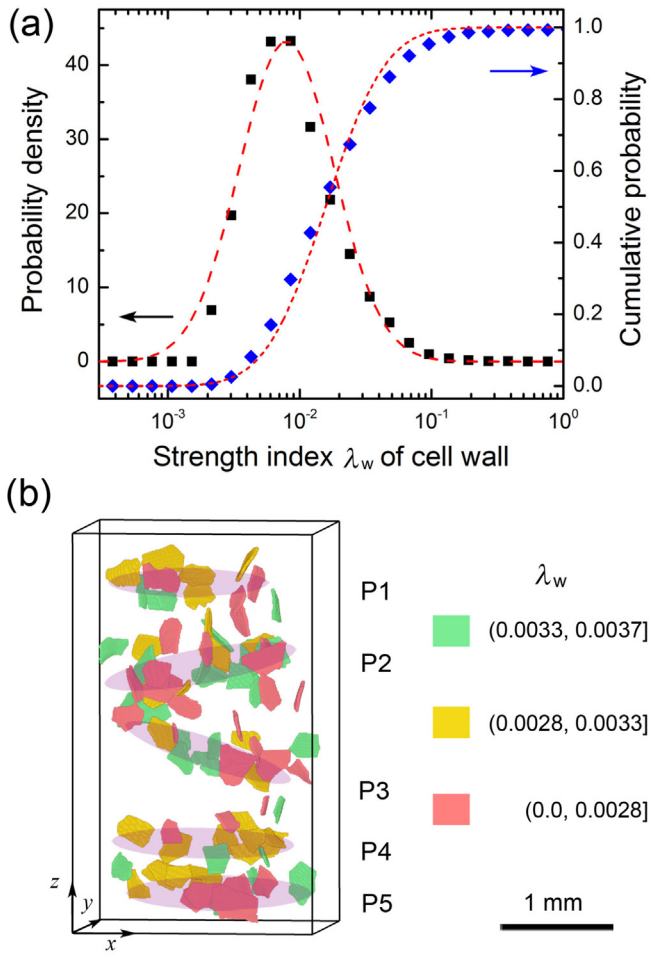

Fig. 4. (a) Probability density and accumulative probability distribution of the buckling strength index λ_w of cell walls. The dashed curves are both lognormal fitting. (b) Spatial distribution of the weakest 3% cell walls. Red, yellow and green indicate three buckling strength ranges, i.e., $\lambda_w \in (0, 0.0028]$, $(0.0028, 0.0033]$, and $(0.0033, 0.0037]$, respectively. Here, the λ_w-values of 0.0028, 0.0033 and 0.0037 correspond to cumulative probabilities of 1%, 2% and 3% (Fig. 4 (a)), respectively.

the collapse stage between the PMI foam (cell wall buckling) and conventional polymer foams (edge buckling [1]).

The thickness, width, height and inclination angle of each cell wall are obtained and used to calculate its buckling strength index λ_w. The probability distribution of λ_w is presented in Fig. 4 (a); it can be described by a lognormal distribution (the dashed curve), denoted as Lognormal (μ, ω), where $\mu = -4.15$ and $\omega = 0.83$ are, respectively, the mean and standard deviation of λ_w's natural logarithm.

Since the weakest cell walls tend to collapse first during quasi-static loading, we explore the spatial distribution of the strength index of the weakest 3% cell walls (Fig. 4 (b)). Red, yellow and green represent three regimes of buckling strength index, i.e., $(0, 0.0028]$, $(0.0028, 0.0033]$, and $(0.0033, 0.0037]$, respectively. Here, $\lambda_w = 0.0028, 0.0033$ and 0.0037 are thresholds corresponding to a cumulative probability of 1%, 2% and 3% (Fig. 4 (a)), respectively. It is interesting to note that these weak walls in the foam are not uniformly distributed across the sample. They are located in five positions (P1–P5) approximately where the five deformation bands nucleate in the experiment (E1–E5, Fig. 2 (a)). The position with the highest density of weak cells, i.e. band P2, corresponds well to the first nucleated band E2.

The buckling strength of the weakest walls in band P2 determines the macroscopic collapse strength of the foam sample. The mean strength index λ_w of the weakest 3% walls in band P2 (Fig. 4 (b)) is about 0.003, and can be used to predict the macroscopic collapse strength according to Eq. (1). The elastic constants of solid PMI are chosen as $E_s = 5200$ MPa and $\nu_s = 0.35$, respectively [30,21]. The ratio of the solid to total section area is considered equal to the relative density. The predicted collapse strength is 0.63 MPa, comparable to the direct measurement (0.89 MPa; Fig. 1 (a)). The buckling strength of these walls are ~15 MPa, far lower than the yield strength of solid PMI (90 MPa), consistent with the elastic-buckling assumption. According to their weak wall densities, bands P5 and P3 should nucleate after band P2, followed by P1 and P4, consistent with the sequence of band nucleation in the experiment (Fig. 1 (b)). Therefore, the cell wall strength index can predict accurately the location and sequence for deformation banding. It also explains why the local low-density area is favored for deformation banding, since the cells in such areas generally have large volume but thin walls, and thus a low buckling strength.

In summary, *in situ* X-ray CT is used to characterize the evolution of 3D microstructures of a closed-cell PMI foam under uniaxial compression. Discrete deformation bands are observed to nucleate in sequence across the sample during the collapse stage. An edge segmentation technique is developed to extract the geometric parameters of cell walls which are then used to calculate their buckling strength index. The probability distribution of the strength index of cells follows a lognormal distribution. The spatial distribution of the strength index of the weakest cell walls can be used to predict position and nucleation sequence of deformation bands. Our results highlight the correlation between cell wall buckling and deformation banding for closed-cell foams, which may serve a basis for tailoring local strength and energy absorption of cellular materials in terms of cell wall morphology.

Acknowledgments

This work was supported by NSFC (Grant Nos. 11802252 and11627901). This research used resources of the Advanced Photon Source, a U.S. Department of Energy (DOE) Office of Science User Facility operated for the DOE Office of Science by Argonne National Laboratory under Contract No. DE-AC02-06CH11357.

Appendix A. Supplementary data

Supplementary data to this article can be found online at https://doi.org/10.1016/j.scriptamat.2019.06.006.

References

[1] L.J. Gibson, M.F. Ashby, Cellular Solids: Structure and Properties, Cambridge University Press. 1999.
[2] V.S. Deshpande, N.A. Fleck, Acta Mater. 49 (2001) 1859–1866.
[3] H. Janik, M. Marzec, Mater. Sci. Eng. C 48 (2015) 586–591.
[4] T.-R. Kim, J.K. Shin, T.S. Goh, H.-S. Kim, J.S. Lee, C.-S. Lee, Compos. Struct. 180 (2017) 686–695.
[5] J. Banhart, Prog. Mater. Sci. 46 (2001) 559–632.
[6] M. Zaiser, F. Mill, A. Konstantinidis, K.E. Aifantis, Mater. Sci. Eng. A 567 (2013) 38–45.
[7] K.A. Issen, T.P. Casey, D.M. Dixon, M.C. Richards, J.P. Ingraham, Scr. Mater. 52 (2005) 911–915.
[8] D.J. Werther, A.J. Howard, J.P. Ingraham, K.A. Issen, Scr. Mater. 54 (2006) 783–787.
[9] Z. Fan, B. Zhang, Y. Gao, X. Guan, P. Xu, Scr. Mater. 142 (2018) 32–35.
[10] K. Issen, J. Rudnicki, J. Geophys. Res.-Sol. Ea. 105 (2000) 21529–21536.
[11] T.W. Barraclough, J.R. Blackford, S. Liebenstein, S. Sandfeld, T.J. Stratford, G. Weinländer, M. Zaiser, Nat. Phys. 13 (2017) 272.
[12] M. Saadatfar, M. Mukherjee, M. Madadi, G.E. Schröder-Turk, F. Garcia-Moreno, F.M. Schaller, S. Hutzler, A.P. Sheppard, J. Banhart, U. Ramamurty, Acta Mater. 60 (2012) 3604–3615.
[13] Y. Sun, X. Zhang, Z. Shao, Q.M. Li, Mater. Sci. Eng. A 688 (2017) 27–39.

[14] G.E. Schröder-Turk, W. Mickel, S.C. Kapfer, M.A. Klatt, F.M. Schaller, M.J.F. Hoffmann, N. Kleppmann, P. Armstrong, A. Inayat, D. Hug, M. Reichelsdorfer, W. Peukert, W. Schwieger, K. Mecke, Adv. Mater. 23 (2011) 2535–2553.
[15] A.F. Bastawros, H. Bart-Smith, A.G. Evans, J. Mech. Phys. Solids 48 (2000) 301–322.
[16] S.A. McDonald, L.C.R. Schneider, A.C.F. Cocks, P.J. Withers, Scr. Mater. 54 (2006) 191–196.
[17] J. Baruchel, J.-Y. Buffiere, P. Cloetens, M. Di Michiel, E. Ferrie, W. Ludwig, E. Maire, L. Salvo, Scr. Mater. 55 (2006) 41–46.
[18] J. Adrien, E. Maire, N. Gimenez, V. Sauvant-Moynot, Acta Mater. 55 (2007) 1667–1679.
[19] B.M. Patterson, N.L. Cordes, K. Henderson, J.J. Williams, T. Stannard, S.S. Singh, A.R. Ovejero, X. Xiao, M. Robinson, N. Chawla, J. Mater. Sci. 51 (2016) 171–187.
[20] B.X. Bie, J.Y. Huang, D. Fan, T. Sun, K. Fezzaa, X.H. Xiao, M.L. Qi, S.N. Luo, Carbon 121 (2017) 127–133.
[21] Q.M. Li, R.A.W. Mines, R.S. Birch, Int. J. Solids Struct. 37 (2000) 6321–6341.
[22] S. Arezoo, V. Tagarielli, N. Petrinic, J. Reed, J. Mater. Sci. 46 (2011) 6863–6870.
[23] D. Gürsoy, C.F. De, X. Xiao, C. Jacobsen, J. Synchrotron Radiat. 21 (2014) 1188–1193.
[24] Y.-H.R. Tsai, S. Osher, Acta Numer. 14 (2005) 509–573.
[25] L. Vincent, P. Soille, IEEE T. Pattern Anal. (1991) 583–598.
[26] A. Criminisi, A. Blake, C. Rother, J. Shotton, P.H.S. Torr, Int. J. Comput. Vision 71 (2007) 89–110.
[27] S. Roux, F. Hild, P. Viot, D. Bernard, Compos. Part A 39 (2008) 1253–1265.
[28] S.P. Timoshenko, M.G. James, Theory of Elastic Stability, Dover Publications. 1961.
[29] C. Harris, M. Stephens, A combined corner and edge detector, Alvey Vision Conference, vol. 15, Citeseer. 1988, pp. 10–5244.
[30] C.R. Siviour, S.M. Walley, W.G. Proud, J.E. Field, Polymer 46 (2005) 12546–12555.